Real-Time Volume Rendering Visualization of Dual-Modality PET/CT Images With Interactive Fuzzy Thresholding Segmentation

Jinman Kim, *Member, IEEE*, Weidong Cai, *Member, IEEE*, Stefan Eberl, *Member, IEEE*, and Dagan Feng, *Fellow, IEEE*

***Abstract*—Three-dimensional (3-D) visualization has become an essential part for imaging applications, including image-guided surgery, radiotherapy planning, and computer-aided diagnosis. In the visualization of dual-modality positron emission tomography and computed tomography (PET/CT), 3-D volume rendering is often limited to rendering of a single image volume and by high computational demand. Furthermore, incorporation of segmentation in volume rendering is usually restricted to visualizing the presegmented volumes of interest. In this paper, we investigated the integration of interactive segmentation into real-time volume rendering of dual-modality PET/CT images. We present and validate a fuzzy thresholding segmentation technique based on fuzzy cluster analysis, which allows interactive and real-time optimization of the segmentation results. This technique is then incorporated into a real-time multi-volume rendering of PET/CT images. Our method allows a real-time fusion and interchangeability of segmentation volume with PET or CT volumes, as well as the usual fusion of PET/CT volumes. Volume manipulations such as window level adjustments and lookup table can be applied to individual volumes, which are then fused together in real time as adjustments are made. We demonstrate the benefit of our method in integrating segmentation with volume rendering in its application to PET/CT images. Responsive frame rates are achieved by utilizing a texture-based volume rendering algorithm and the rapid transfer capability of the high-memory bandwidth available in low-cost graphic hardware.**

***Index Terms*—Dual-modality positron emission tomography and computed tomography (PET/CT), fuzzy C-means cluster analysis, interactive three-dimensional (3-D) segmentation, multi-volume rendering, real-time volume rendering.**

I. Introduction

ADVANCES in digital medical images are resulting in increased image volumes from the acquisition of four-dimensional (4-D) imaging modalities, such as dynamic positron emission tomography (PET), and dual modality PET and computed tomography (PET/CT). These images have introduced significant challenges for efficient visualization [1]–[3]. In line with the advances in image acquisition, three-dimensional (3-D) visualization algorithms have been developed that enable real-time visualization of multidimensional volumes using low-cost hardware instead of restricting it to high-end expensive workstations [4]–[6]. 3-D visualization has become an attractive method for imaging applications, including image-guided surgery and radiotherapy, and computer-aided diagnosis [3], [4], [7]–[12]. In these applications, segmentation is often employed, which enables visual separation and selection of specific volumes of interest (VOIs) [6], [12]–[18]. Segmentation of the image volume can be performed manually by a physician. However, such delineation is subjective, and hence, may not be reproducible, and it is time consuming. Fully automated methods can only be applied successfully within precisely defined bounds and they cannot guarantee accurate delineation under all circumstances, thus requiring some kind of operator intervention, such as in interactive segmentation.

Studies involving interactive segmentation in 3-D visualization have often been limited to rendering the preprocessed segmentation results [16]–[18]. However, these methods render only the segmented VOIs, without placing them in the context of surrounding structures. In [18], a method of correcting segmentation errors from volume-rendered VOIs by adjusting the radius of the viewable volume to reveal the surrounding image was presented. Although this method allows a physician the ability to correct for segmentation errors in volume rendering, it was limited to only rendering the surrounding voxels within the radius of the VOIs and did not take into consideration that the surrounding voxels may have no relation to the VOI.

These interactive segmentation methods were all based on visualization of a single volume of images. In dual-modality PET/CT images, which consist of co-registered functional and anatomical image volumes, the ability to visualize the segmentation result with both image volumes can be of considerable benefit. For instance, segmentation of tumor structures from low-resolution, functional PET image data can benefit from overlaying it on the CT to provide an anatomical frame of reference and precise localization.

In this paper, we investigated and validated the incorporation of interactive segmentation into real-time 3-D visualization of PET/CT images. We present a fuzzy thresholding segmentation method for PET images in real-time volume rendering. In the segmentation of functional PET images, cluster analysis

Manuscript received August 22, 2005; revised December 24, 2005. This work was supported in part by the ARC and RGC grants.

J. Kim and W. Cai are with the Biomedical and Multimedia Information Technology Group, School of Information Technologies, University of Sydney, Sydney, NSW 2006, Australia (e-mail: jinman@it.usyd.edu.au).

S. Eberl is with the Biomedical and Multimedia Information Technology Group, School of Information Technologies, University of Sydney, Sydney, NSW 2006, Australia, and also with the Department of PET and Nuclear Medicine, Royal Prince Alfred Hospital, Sydney, NSW 2050, Australia.

D. Feng is with the Biomedical and Multimedia Information Technology Group, School of Information Technologies, University of Sydney, Sydney, NSW 2006, Australia, and also with the Center for Multimedia Signal Processing, Department of Electronic and Information Engineering, Hong Kong Polytechnic University, Kowloon, Hong Kong.

Digital Object Identifier 10.1109/TITB.2006.875669

based on kinetic behavior has previously been found effective in classifying kinetic patterns [19]–[21], including segmentation of regions of interest [19], and the generation of parametric images from huge data sets [20]. In these approaches, PET images were partitioned into a predefined number of cluster groups based on "crisp" clustering, where one voxel was assigned to a single cluster group. The fuzzy extension to the crisp clustering, such as the fuzzy C-means (FCM) cluster analysis [22], presents the advantage of assigning probabilities of each voxel belonging to a particular cluster. This attribute is utilized in this paper to control the segmentation by simple and computationally efficient thresholding of the cluster probabilities. We describe and evaluate a fuzzy thresholding technique and its integration into an interactive multi-volume viewer (IMV^2) is demonstrated. The IMV^2 allows fusion of the segmentation with PET or CT images as well as the usual fusion of PET and CT images. Volume manipulation tools designed for PET/CT visualization and which allow manipulation of individual volumes, e.g., thresholding the CT and adjusting window levels of PET images are incorporated. The resultant manipulated volumes are then fused together in real time as the adjustments are made.

II. Method

The IMV^2 consists of four major steps as shown in the flowchart in Fig. 1: 1) segmentation of PET images using FCM cluster analysis into cluster groups based on functional similarity; 2) volume rendering of PET, CT, and segment data using texture-based rendering technique; 3) interactive fuzzy thresholding of PET data with real-time volume rendering of dual-modality PET/CT; and 4) volume manipulation tools such as window level adjustments and lookup table (LUT) applied to PET/CT volume rendering.

A. Automated 4-D FCM Cluster Analysis of Dynamic/Static PET Images

Prior to segmentation, the image data are preprocessed as follows: low-count background areas in the PET images are removed (set to zero) by thresholding. Isolated voxels and gaps are then removed and/or filled by a $3 \times 3 \times 3$ morphological opening filter followed by a closing filter. For dynamic PET data, tissue time activity curves (TTACs) are extracted for each nonzero voxel to form the kinetic feature vector $\mathbf{f}(t)$ of time interval $t(t = 1, 2, \ldots, T)$, where T is the total number of time points. For static images, a single frame is acquired at $t = T$.

The FCM cluster analysis based on [22] is applied to assign each of the N feature vectors to one of a set number C of distinct cluster groups. For each cluster, centroids are assigned as the feature vectors of distinct, randomly selected voxels. The value of each centroid voxel is replaced with the average of the $3 \times 3 \times 3$ surrounding voxels to avoid false selection of a noisy outlier that may result in a cluster with a single member. FCM cluster analysis minimizes the objective function J, according to

$$J = \sum_{i=1}^{N} \sum_{j=1}^{C} u_{ij}^{P} D\left(\mathbf{f}_i(t), \bar{\mathbf{f}}_{c_j}(t)\right)^2 \tag{1}$$

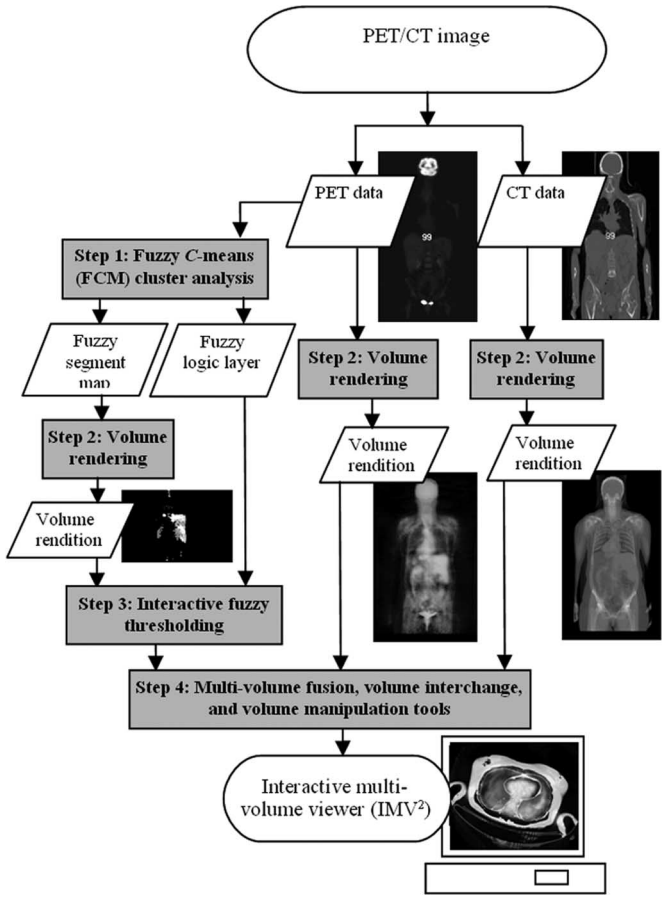

Fig. 1. Flowchart of the proposed interactive multi-volume visualization. After segmenting the PET image using FCM cluster analysis (step 1), the segmentation map and fuzzy logic layer are constructed. The segmentation map, PET, and CT image volumes are rendered using texture-based volume rendering (step 2). The fuzzy logic layer is then used to interactively adjust the rendered segmentation volume by fuzzy thresholding (step 3). These volumes can be fused and interchanged in real time with volume manipulation tools (step 4) included in the IMV^2.

where $P(1 \leq P \leq \infty)$ is a weighting exponent on each fuzzy membership, which determines the amount of fuzziness of the resulting classification, and u_{ij} is the membership degree of the ith feature vector in the cluster j. The similarity measure between the ith feature vector $\mathbf{f}_i(t)$ and the cluster centroid $\bar{\mathbf{f}}_{c_j}(t)$ of the jth cluster group c_j was calculated using the Euclidean distance D_{ij} given by

$$D\left(\mathbf{f}_i, \bar{\mathbf{f}}_{c_j}\right) = \left[\sum_{t=1}^{T} s(t)\left(\mathbf{f}_i(t) - \bar{\mathbf{f}}_{c_j}(t)\right)^2\right]^{1/2} \tag{2}$$

where $s(t)$ is a scale factor of time point $t(t = 1, 2, \ldots, T)$ equal to the duration of the tth frame divided by the total dynamic acquisition time. The scale factor $s(t)$ gives more weight to the longer frames, which contain more reliable data. The minimization of J is achieved by iteratively updating the u_{ij} and the cluster centroids $\bar{\mathbf{f}}_{c_j}(t)$ with

$$u_{ij} = \frac{1}{\sum_{k=1}^{C}\left[\frac{D\left(\mathbf{f}_i(t), \bar{\mathbf{f}}_{c_j}(t)\right)}{D\left(\mathbf{f}_i(t), \bar{\mathbf{f}}_{c_k}(t)\right)}\right]^{\frac{2}{P-1}}} \tag{3}$$

$$\bar{\mathbf{f}}_{c_j}(t) = \frac{\sum_{i=1}^{N} u_{ij}^{P} \mathbf{f}_i(t)}{\sum_{i=1}^{N} u_{ij}^{P}}. \tag{4}$$

Thus, a probabilistic fuzzy membership degree is assigned to every voxel i, such that $\sum_{j=1}^{C} u_{ij} = 1.0$. The procedure is terminated when the convergence criterion ε in the range of [0, 1] is satisfied, i.e.,

$$\max_{ij} \left\{ \left| u_{ij}^{m+1} - u_{ij}^{m} \right| \right\} < \varepsilon \tag{5}$$

where m is the iteration step. Upon termination, the segmentation map image is constructed by assigning each voxel to the cluster for which it has the highest membership degree. The optimal number of clusters is determined using the fuzzy validation measure [23] S given by

$$S = \frac{\sum_{j=1}^{C} \sum_{i=1}^{N} u_{ij}^{P} \left\| \bar{\mathbf{f}}_{c_j}(t) - \mathbf{f}_i(t) \right\|^2}{N \min_{ij} \left\| \bar{\mathbf{f}}_{c_j}(t) - \bar{\mathbf{f}}_{c_i}(t) \right\|^2} \tag{6}$$

and is evaluated for integer values of C in the range $(L - 3 < C < L + 4)$, where L is the number of tissue types expected to be present. Smaller value of S indicates a cluster scheme with more compact and more separate clusters. Values of the parameters C, P, and ε are empirically determined (see Section III).

B. Fuzzy Membership Degree Layer and Fuzzy Thresholding

From each segmented cluster $c_j (j = 1, 2, \ldots, C)$, a fuzzy membership layer l_j is constructed consisting of the membership degrees u_{ij} for all N voxels to c_j, as shown in Fig. 2(1). The u_{ij} are scaled to 0%–100% for the membership layer. For each membership layer, a fuzzy histogram can be plotted as in Fig. 2(2), which represents the membership of the voxels to a cluster. The fuzzy thresholding works by controlling the fuzzy membership threshold of a selected cluster. By lowering the fuzzy threshold from the automated FCM segmentation threshold, additional voxels with weaker membership to the cluster centroid can be assigned to the cluster. On the other hand, by increasing the fuzzy threshold, fewer voxels, but with higher membership, are clustered. With dynamic PET images, the fuzzy thresholding affects the voxels that are similar in kinetic behavior to the cluster centroid. For static PET images, the fuzzy thresholding is similar to intensity-based thresholding.

C. Real-Time Multi-Volume Rendering Overview

In IMV^2, visualization tools were designed to provide physicians with efficient ways to interpret and navigate through the dual-modality PET/CT images. The main features of IMV^2 are illustrated in Fig. 3 with the use of whole-body PET/CT image. From the PET, CT, and segmentation volumes, any volume can be rendered individually or two volumes can be selected and fused together, with the ability to interchange the volumes and the fusion ratio of the volumes in real time. The segmentation volume allows for interactive selection of different clusters and fuzzy thresholding. The rendered volume(s) can be interactively navigated using conventional volume navigation tools including rotation, scaling, and translation. To remove a portion

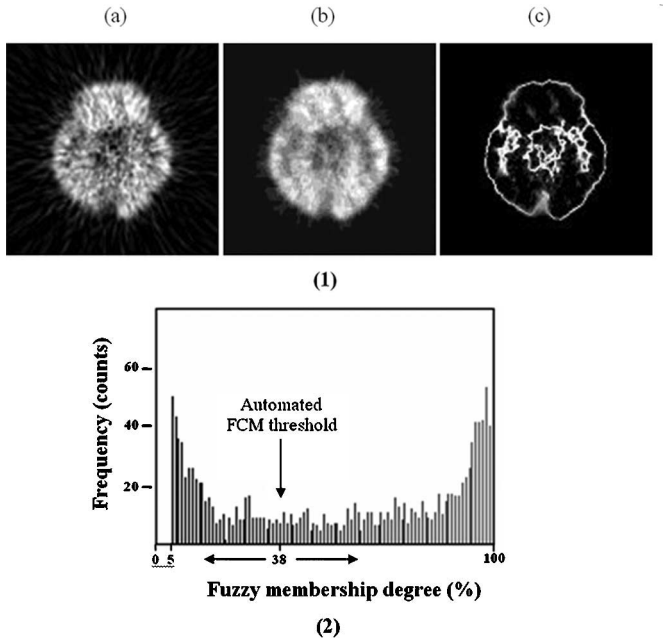

Fig. 2. (1) Result from applying FCM segmentation to a clinical brain PET study: (a) Original image. (b) FCM segmentation map. The clusters from the automated segmentation map are assigned to a shade of gray corresponding to the cluster average. (c) Fuzzy logic layer of a selected cluster #1. The fuzzy membership layer is also assigned to a shade of gray in an ascending order of membership degree. (2) Histogram distribution of the fuzzy membership degree of voxels in (c). First 5% of the fuzzy membership histogram, consisting of a large number of voxels that have minor relationships to the cluster, is removed for presentation purposes.

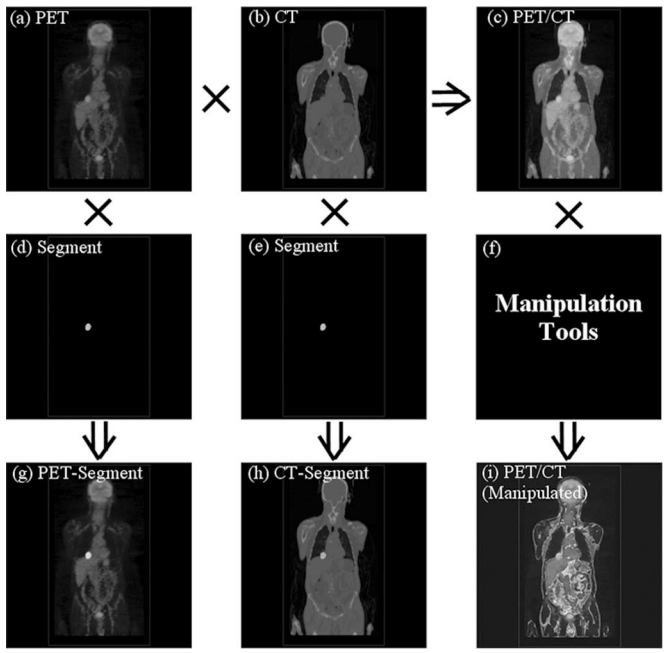

Fig. 3. Overview of the main features in the proposed interactive multi-volume visualization. Individual volumes can be rendered (a) and (b) or can be combined with another volume, such as PET/CT (c). Combination of volumes and the ability to interchange the volumes in real time allows the segmented VOI of a tumor (d) and (e) to be fused and visualized with PET (g) and CT (h). The VOI is displayed using the white LUT for presentation purpose. Volume manipulations can be applied to individual volumes with the volumes being fused and the volume rendered in real time as shown in (i) where the CT has been thresholded to reveal the lung boundary surrounding the tumor.

of the volume that may obscure the user's view, a "volume clipping" tool can be applied by using a plane that cuts through the volume perpendicular to the viewing window. Alternatively, the user can position a "clipping box" that encapsulates the volume such that only the volume residing inside the box is visible. The ability to clip the volume, together with volume navigation, allows the user to explore the large multi-volume data by interactively selecting the viewing window, which isolates the interested section from the whole volume. Another tool is the "adaptive sampling rate" that allows the volume to be sampled at a lower rate to increase the responsiveness to movement, which are necessary when dealing with large multidimensional volumes. When the movement is completed, the samples are raised back to the default setting of fully sampled data. The sampling rate is the number of parallel planes used in texture-based volume rendering to render the volume (see Section II-D). Other tools include "window-level adjustment", "transfer function", "LUT", and "intensity-based thresholding". CT images, which occupy greater dynamic range than is possible to display simultaneously, can be interactively adjusted using the window level. Transfer function can be used to control the opacity of the volume, such that particular voxels (measured in the voxel's intensity) become more prominent. In addition, intensity-based thresholding can be applied to potentially segment out the tissue structures in CT [24] that are acquired in high resolution and contain well-defined separation of tissue structures. As the PET and CT volumes are rendered independently, manipulations can be applied to individual volumes, e.g., thresholding the CT and adjusting window levels of PET data, and the resultant manipulated data sets are then fused together in real time as the adjustments are made.

D. *Interactive* IMV^2 *Implementation*

The IMV^2 has been developed using the OpenGL [25] and SGI Volumizer 2.7 application programming interface (API) [26] to render the multi-volume images using texture-based volume rendering [5], [6], [27], [28]. The texture-based volume rendering creates parallel planes through the columns of the volume data, in the principal direction most perpendicular to the user's line of sight, which are then drawn back-to-front with appropriate 3-D texture coordinates [5]. IMV^2 utilizes the high-capacity memory bandwidth of low-cost graphic hardware to perform a rapid transfer of the 3-D textures from the system memory into the graphic memory. By utilizing the large bandwidth, the volume interchange method replaces an old volume in the graphic memory with a new volume. The two volumes are fused using the hardware-based per-voxel fusion method [29] of compositing the two voxels from respective volumes to create a new voxel in real time. This method does not require any preprocessing of the volume data and thus allows real-time adjustment of the fusion ratio of PET to CT. The segmentation volume is interactively adjusted in real time by assigning transparency values to the voxels based on the fuzzy threshold. In this approach, voxels that have greater fuzzy membership than the defined threshold are assigned to a visible transparency level and other voxels are set to fully transparent.

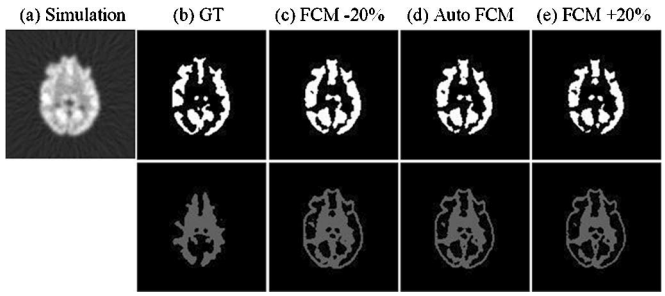

Fig. 4. (a) Normal noise level simulation (last temporal frame). In (b)–(e), the top row is the GM and bottom row is the WM. (b) GT. (c) Fuzzy threshold of 28% for GM and 30% for WM. (d) Automated FCM segmentation with threshold of 48% for GM and 50% for WM. (e) Fuzzy threshold of 68% for GM and 70% for WM.

III. Evaluation and Experimental Results

A. *Validation of FCM Segmentation—Computer Simulations*

Computer simulations were performed to evaluate the performance and reliability of the fuzzy thresholding segmentation. The anatomical Zubal brain phantom [30] was reduced to white matter (WM) and gray matter (GM) and 20 cross-sectional slices. A five-parameter 2-[18F] fluoro-2-deoxy-D-glucose (18F-FDG) model [31] was used to simulate realistic TTAC values to construct 22 temporal frame sequences. Each slice was smoothed by applying a Gaussian filter with a full-width-half maximum (FWHM) of 8 mm prior to forward projection. Projections were scaled to three different count levels by applying a scale factor that sets the maximum pixel count in the last frame to 100 (high noise), 500 (normal noise), and 800 (low noise) counts, where 500 was the maximum observed in comparable clinical studies. Poisson noise was then added to the scaled projection data, which were reconstructed using filtered backprojection with a *Hann* filter. Noise-free ground truth (GT) images were constructed by smoothing the phantom data with Gaussian blur as in the noisy simulations. Voxels mixed at the boundary in the smoothed images were reclassified to the tissue with the highest contribution. For boundaries separating tissue from zero count regions such as ventricles, 40% of the tissue counts were defined.

The fuzzy thresholding results of GM (first row) and WM (second row) are illustrated in Fig. 4. From visual inspection, the GM segmentation result resembles the GT in Fig. 4(b) most closely with the increased threshold shown in Fig. 4(e). The reverse was evident for WM where the fuzzy thresholding result in Fig. 4(c) is visually the most similar to its GT. This illustrates the ability of the fuzzy thresholding to interactively optimize the segmentation result for particular structures of interest. The ring artifact around the periphery of the WM segmentation is attributed to the mixed tissue contribution between the GM and the background. In the FCM cluster analysis, the background was removed by using the boundaries of the tissue structures defined in the Zubal phantom and two clusters were applied corresponding to the WM and GM. Empirically derived cluster analysis parameter values of $P = 2.0$, and $\varepsilon = 0.1$ gave acceptable results. The segmentation results were found to be quite

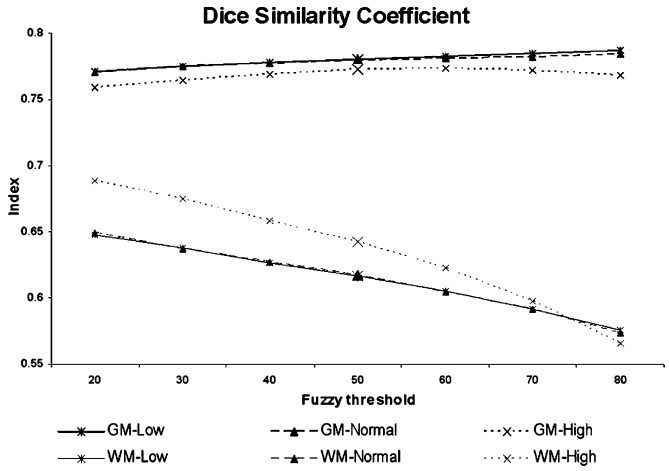

Fig. 5. Results of quantitative evaluation measures applied to the simulations at the three noise levels (low, normal, and high). Automated FCM segmentation thresholds are represented by the enlarged data points. The thresholds for the normal noise level were between 18% and 78% for WM, and 20% and 80% for GM (±30% from automated FCM) in increments of 10%. The low noise level had the same threshold, and the high noise level was different only in WM, which was 19%–79%.

insensitive to these two parameters. Quantitative evaluation of the application of fuzzy thresholding was performed with dice similarity coefficient (DSC) [32] given as

$$\mathrm{DSC} = 2|A_{\mathrm{Est}} \cap A_{\mathrm{True}}|/(|A_{\mathrm{Est}}| + |A_{\mathrm{True}}|) \qquad (7)$$

which measures the spatial overlap between the estimated and true segmented areas. The DSC is in the range of [0, 1], where 1 represents two overlapping areas of identical size and location. Fig. 5 shows the evaluation measures of the simulation study for the three noise levels as a function of fuzzy thresholding levels. Based on these results, the DSC improved with increasing fuzzy threshold for the GM in both the low and normal noise levels. For the high noise level, the automated threshold was optimal for GM segmentation. In WM, decreasing the threshold showed a marked improvement in DSC among all noise levels. This suggests that the automated segmentation has over-segmented the GM and under-segmented the WM, which was in accordance with the visual findings in Fig. 4. The results indicate that the proposed fuzzy thresholding was most effective at high noise levels and that the method was robust in terms of noise.

B. Application of FCM to Clinical 4D Dynamic Brain Pet Study

The fuzzy thresholding was applied to dynamic clinical ^{18}F-FDG brain PET studies. The dynamic images were decay corrected to the time of injection and attenuation corrected, and then reconstructed using filtered backprojection with a Shepp and Logan filter. Segmentation of a patient study with a tumor is shown in Fig. 6(1). The FCM cluster analysis automatically separated the prominent tissue structures with a clear indication of the tumor (left center of the image). The application of fuzzy thresholding to a selected tumor structure shown in Fig. 6(2) demonstrates the addition or removal of only the voxels based on the kinetic similarity of the TTACs to the cluster centroid, allowing interactive optimization of the segmentation results and

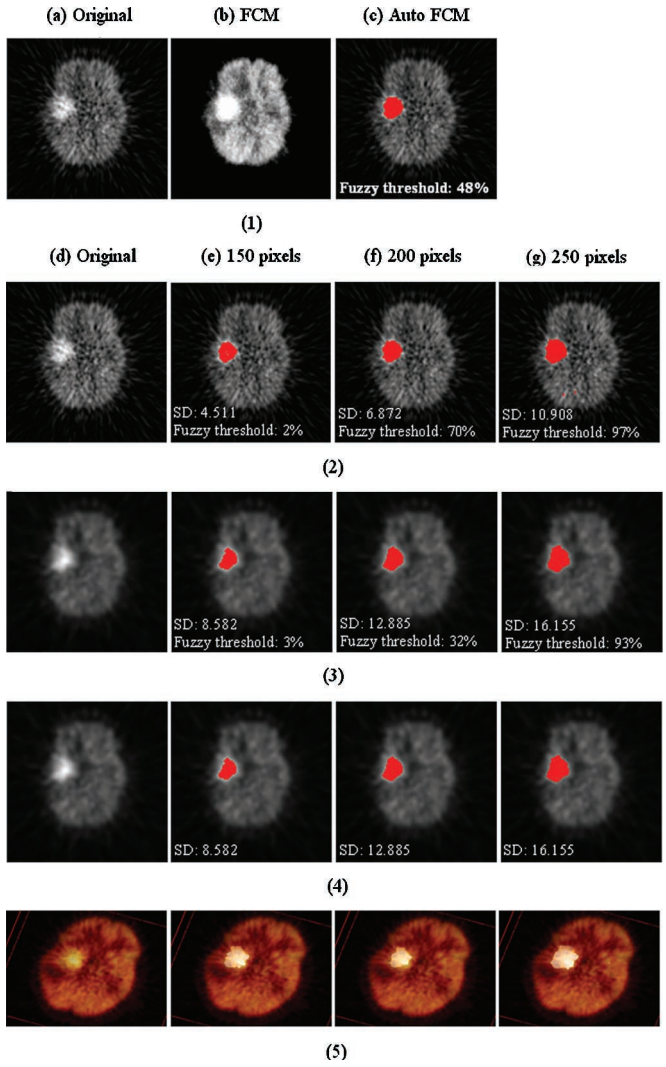

Fig. 6. Segmentation applied to clinical dynamic PET patient study and parametric images. (1) Traverse slice 21 (a) with FCM segmentation result (b) and the selection of a tumor cluster (c). (2) Fuzzy thresholding applied to dynamic PET image. (3) Fuzzy thresholding and (4) Conventional thresholding of Patlak parametric image. (5) Volume rendering of results in row (2).

tumor volume definition. Standard deviation of the Euclidean distance measures given in (2) between the voxel's TTAC feature vectors and their thresholded cluster centroid was treated as an indicator of the homogeneity of the structure. Based on the result in Fig. 6(2), as the threshold was increased, a tighter volume around the tumor was selected and the standard deviation was lowered, which demonstrates that the lowering of the threshold resulted in the clustering of voxels that were more homogeneous.

To demonstrate that the technique could also be applied to parametric images, parametric images were generated with voxel by voxel Patlak graphical analysis plot [33] and the measured arterial plasma concentration of the tracer. Due to the high noise in the Patlak plot images, a Gaussian filter with an FWHM of 7.5 mm was applied. The Patlak parametric images were then segmented with FCM technique [Fig. 6(3)] as well as intensity-based thresholding [Fig. 6(4)]. For each

of the techniques, parameters were adjusted to give tumor segment volumes of 150, 200, and 250 voxels [Fig. 6(e)–(g), respectively]. As expected, for static images, such as the Patlak parametric images, FCM segmentation provides results analogous to simple intensity threshold-based segmentation. Interestingly, as indicated by the higher standard deviations compared to the FCM segmentation of the dynamic data [Fig. 6(2)], the Patlak analysis does not group the TTAC curves, which were most similar as defined by the Euclidean distance, and hence results in a different definition of tumor volume compared to FCM applied directly to the dynamic data. This is likely due to the Patlak analysis reflecting different characteristics of the dynamic curve and effectively giving different weighting to different parts of the TTAC than that used for estimating the Euclidean distance between the TTACs. The most appropriate data to use (parametric images, dynamic data, or selected static images) will depend on the application and the characteristics, which are required to be featured in the segmented volume.

The volume rendering of the segmented cluster and the thresholded results are presented in Fig. 6(5). The PET image and the segmentation results were individually volume rendered and then fused together with equal fusion ratios.

In the FCM segmentation of dynamic PET and Patlak images, the background threshold was set at 15% of the maximum counts in each slice of the summed temporal frames. This threshold value was found not to be critical and moderate changes ($\pm 5\%$) had little effect on the results. As in the simulations, the FCM cluster analysis parameters P and ε were set to 2.0 and 0.1, respectively. The number of clusters C was determined from the fuzzy validation measure S given in (6). For the dynamic PET, as C was increased from 5 to 12, the values of S was increased gradually up to $C = 8$ (maximum increase of 28% from the previous S), followed by a rapid increase at $C = 9$ (increase of 113%) with gradual increase in S thereafter (maximum increase of 26%). Although a small value of S indicates a cluster scheme with well-defined clusters, to maximize the partition of the individual tissue types, the optimal number of clusters was taken to be the value of C corresponding to the value of S prior to the rapid increase. Similarly, $C = 7$ was found optimal for the Patlak image.

C. Clinical Whole-Body PET/CT Study

Fig. 7 demonstrates a potential application of IMV^2 in interactively visualizing and segmenting out tumor volumes from a whole-body PET/CT image. The reconstructed PET/CT images were 128×128 with voxel dimensions of $5.148 \times 5.148 \times 3.375$ mm for PET, and 512×512 with voxel dimensions of $0.977 \times 0.977 \times 3.4$ mm for CT. PET and CT images were cropped and rescaled to 256×256 with voxel dimensions of $1.953 \times 1.953 \times 3.4$ mm. The automated segmentation of the tumors fused with the PET volume is shown in Fig. 7(b). The FCM cluster analysis has identified the two regions with tumors when compared to the PET/CT counterpart in Fig. 7(a). The segmentation of the tumors can be interactively optimized by increasing the fuzzy threshold as shown in Fig. 7(c), which resulted in the reduction in the size of the segmented tumors. The reduced size was attributed to only selecting voxels that have the highest membership to the cluster containing the tumor. This ability provides the physician with control over the definition of the viable tumor volume, for example, for radiotherapy treatment planning while avoiding the tedium and time associated with manually defining a 3-D VOI. The real-time rendering of the segmentation with either PET or CT image data provides quick and effective feedback on the accuracy of the segmented tumor volume as the fuzzy threshold is adjusted. The fusion of the segmented tumors on the CT is shown in Fig. 7(d). This permits improved visualization of the anatomical frame of reference and localization of the segmented tumors when compared to the fusion of PET/CT in Fig. 7(a). The transparency level and the LUT of the segmented volumes can be adjusted to reduce obscuration of underlying structures relevant for the interpretation of the images and segmentation result. Other segmented clusters representing different functional structures such as the lung, can be interactively selected and thresholded. For this example, the FCM cluster analysis was applied to a subsection of the whole-body PET images (30 slices), the background threshold was set at 10%, and the number of clusters $C = 4$ was determined to be optimal.

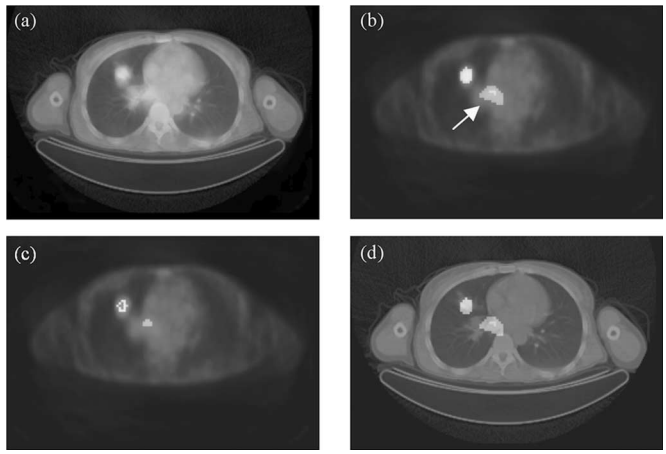

Fig. 7. (a) Volume rendering of PET/CT image. (b) Automated FCM segmentation result with segmented tumor structures fused with PET. Fuzzy threshold of the selected cluster was at 56%. (c) Reduced segmentation of the tumor resulting from increase in fuzzy threshold to 91%. (d) Segmentation result of (b) fused with CT. All volumes have been fused with equal fusion ratios.

Fig. 8 illustrates some of the tools available in IMV^2. In Fig. 8(a), an example of intensity-based thresholding of CT structures is illustrated. The thresholded CT results were volume rendered together with PET, which revealed the boundary of the anatomical structure fused with PET. Fig. 8(b) illustrates an example of window-level-adjusted PET (brighter) fused with the CT, which has been intensity thresholded as in Fig. 8(a). In Fig. 8(c), window-level-adjusted CT (showing lung vasculature) fused with PET is shown. Finally, Fig. 8(d) shows the clipped PET/CT image using the clipping box, revealing internal structures of the fused PET/CT image.

A major goal of the IMV^2 is to provide real-time volume rendering to allow real-time manipulations. Table I shows measured times for various manipulations in IMV^2, running on ATI

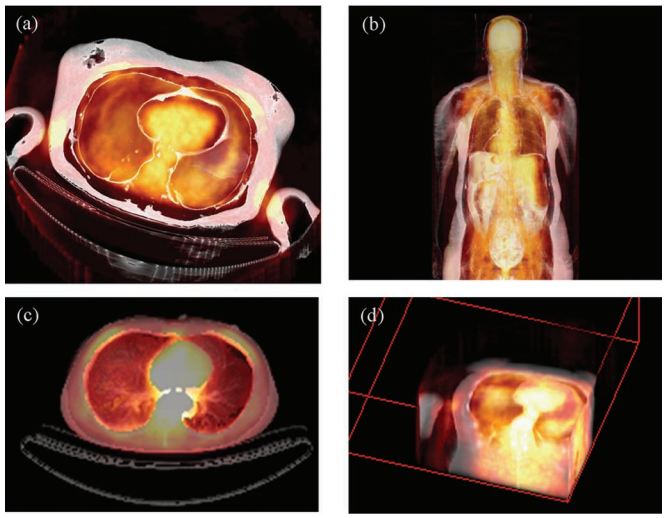

Fig. 8. Various manipulations applied to PET/CT volume renditions. (a) Intensity thresholding of CT to show the lung boundary, fused with PET. (b) Window level applied to PET and intensity thresholding applied to CT images. (c) Window-level-adjusted CT (showing lung vasculature) fused with PET. (d) Clipped PET/CT (clipping box) with window-level adjustments.

TABLE I
AVERAGE FRAME RATES MEASURED IN FRAMES PER SECOND (FPS) FOR VARIOUS PET/CT MANIPULATIONS IN IMV^2

Manipulation	Data Set	Average FPS
Rotation	PT-CT	4.8
Rotation	PT or CT	10.9
Clip (slice)	PT-CT	15.0
Clip (box)	PT-CT	6.3
Window level	CT	6.2
Intensity threshold	PT-CT	4.4
Zoom	PT-CT	4.0
Fuzzy threshold	PT-SM	11.7

Key: PT = PET, SM = Segmentation.

Radeon 9600 graphics hardware with 64 MB of memory, applied to subsections of the whole-body PET/CT images with dimensions scaled to $256 \times 256 \times 40$ in 16 bit, and the corresponding segmentation volume in 8 bit. The sampling rate of $1.8 \times 1.8 \times 3.2$ and window size of 500×500 were applied. The rendered volumes can be animated, with good response times of $4 \sim 15$ frames per second (FPS). The time taken for changing different clusters on the segmentation results and the interchange of volumes were measured to have response times of less than 0.5 s. With adaptive sampling rates, where the sampling rate was lowered to $0.6 \times 0.6 \times 0.6$, FPS for all of the manipulations were improved by an average of 5.1 times. An increase in window size to 1000×1000 pixels (double) resulted in a 1.8 times decrease in FPS. Manipulations applied to a whole-body PET/CT were within $1 \sim 3$ FPS. Nonetheless, with the utilization of adaptive sampling rates, the whole-body PET/CT was able to be interactively visualized.

IV. DISCUSSION

This paper described a new visualization method for multi-volume images with the integration of interactive fuzzy thresholding segmentation. Through manual intervention in 3-D visualization, optimization of segmentation parameters was possible to emphasize VOIs and adjust for inter-patient difference. In the segmentation of functional images, partial volume effects (PVEs) caused by limited spatial resolution, and low counting statistics have a significant influence on segmentation errors. Using our fuzzy thresholding, some of these limitations can potentially be overcome. Voxels, which may be incorrectly segmented, often exhibit low fuzzy membership to all clusters, and thus, are most likely to be detected and corrected by changes to the fuzzy threshold. Furthermore, segmentation errors arising from a suboptimal cluster number selection may also be corrected using fuzzy thresholding, i.e., a structure that is separated into two or more cluster groups due to an excessive number of clusters could be manually combined into a single cluster by decreasing the fuzzy threshold of the cluster most representative of the structure.

The determination of the optimum number of clusters for the application of FCM cluster analysis on whole-body PET images was difficult due to the low spatial resolution and the high variation of the tracer uptakes inside the organs. The cluster validity measure in (6) was found to result in an excessive number of clusters, causing the separation of a particular structure into two or more cluster groups, rather than a single cluster representing the structure. However, the use of subsections of the whole-body images (<40 cross-sectional slices) was found to dramatically improve the determination of the optimum number of clusters without causing the separation of structures. Thus, segmentation of VOI in IMV^2 can be applied to subsections of the whole-body image to improve the performance of the segmentation.

FCM segmentation with thresholding was selected as the segmentation method of choice for the following reasons. Once cluster membership probabilities are assigned to each voxel, the FCM thresholding shares the computational efficiency of simple intensity-based thresholding, which is essential to provide a real-time interactive segmentation manipulation. However, unlike simple intensity-based thresholding, it can be applied directly to dynamic data. For static data, it provides segmentation analogous to threshold-based segmentation for regions with the highest uptake such as the tumor examples shown. However, it is potentially more adapted in segmenting out structures that do not have the highest activity uptake, which is more challenging for intensity threshold-based segmentation methods. The proposed multi-volume visualization method is not limited to the FCM segmentation method. Indeed, it can take the input of any segmentation map image that contains labeled voxels corresponding to the segmented VOIs to construct the segmentation volume for visualization. As the updates to the segmentation parameter usually involve only the addition and deletion of voxels to the segmentation volume, the application of interactive segmentation can easily be accommodated using the IMV^2.

V. CONCLUSION

We have demonstrated a multi-volume visualization of dual-modality PET/CT images with integrated fuzzy thresholding segmentation. Our method has the advantage that

the segmentation volume can be fused with PET or CT, as well as the fusion of PET/CT in real-time volume rendering. The ability to visualize and interactively optimize segmentation of PET images that is overlaid on CT images in real-time volume rendering can potentially facilitate VOI generation for applications such as radiotherapy or image-guided surgery. Unlike fully automated techniques, the interactive fuzzy thresholding technique allows the physician to control segmentation while navigating through the rendered PET/CT volumes, without incurring the time penalty associated with manual VOI definition. Overall, the IMV^2 performed well on low-cost graphic hardware prior to software optimization, and we intend to further refine this technique and potential clinical applications in future work.

REFERENCES

[1] M. N. Wernick and J. N. Aarsvold, *Emission Tomography—Fundamentals of PET and SPECT*. London, U.K.: Elsevier, 2004.

[2] R. A. Robb, "Visualization in biomedical computing," *Parallel Comput.*, vol. 25, pp. 2067–2110, 1999.

[3] O. Ratib, "PET/CT image navigation and communication," *J. Nucl. Med.*, vol. 45, pp. 46S–55S, 2004.

[4] A. Rosset, L. Spadola, and O. Ratib, "OsiriX: An open-source software for navigating in multidimensional DICOM images," *J. Digital Imag.*, vol. 17, pp. 205–216, 2004.

[5] P. Bhaniramka and Y. Demange, "OpenGL volumizer: A toolkit for high quality volume rendering of large data sets," in *Proc. Symp. IEEE/ACM SIGGRAPH Volume Vis. Graph.,* Oct. 28–29, 2002, pp. 45–53.

[6] M. Hadwiger, C. Berger, and H. Hauser, "High-quality two-level volume rendering of segmented data sets on consumer graphics hardware," in *Proc. IEEE Vis.,* Oct. 19–24, 2003, pp. 301–308.

[7] R. Shahidi, R. Tombropoulos, and R. P. Grzeszczuk, "Clinical applications of three-dimensional rendering of medical data sets," *Proc. IEEE*, vol. 86, no. 3, pp. 555–568, Mar. 1998.

[8] F. Beltrame, G. De Leo, M. Fato, F. Masulli, and A. Schenone, "A three-dimensional visualization and navigation tool for diagnostic and surgical planning applications," in *Proc. SPIE Vis., Display Image-Guided Procedures*, 2001, vol. 4319, 2001, pp. 507–514.

[9] I. F. Ciernik, E. Dizendorf, B. G. Baumert, B. Reiner, C. Burger, J. B. Davis, U. M. Lütolf, H. C. Steinert, and G. K. Von Schulthess, "Radiation treatment planning with an integrated positron emission and computer tomography (PET/CT): A feasibility study," *Int. J. Radiol. Oncol. Biol. Phys.*, vol. 57, pp. 853–863, 2003.

[10] A. B. Jani, J.-S. Irick, and C. Pelizzari, "Opacity transfer function optimization for volume-rendered computed tomography images of the prostate1," *Acad. Radiol.*, vol. 12, pp. 761–770, 2005.

[11] Y. C. Loh, M. Y. Teo, W. S. Ng, C. Sim, Q. S. Zou, T. T. Yeo, and Y. Y. Sitoh, "Surgical planning system with real-time volume rendering," in *Proc. IEEE Int. Workshop Med. Imag. Augmented Reality,* Jun. 10–12, 2001, pp. 259–261.

[12] D. T. Gering, A. Nabavi, R. Kikinis, W. E. L. Grimson, N. Hata, P. Everett, F. Jolesz, and W. M. Wells, "An integrated visualization system for surgical planning and guidance using image fusion and interventional imaging," in *Proc. Med. Image Comput. Comput. Assisted Intervention*, 1999, pp. 809–819.

[13] H. Hauser, L. Mroz, G. I. Bischi, and M. E. Gröller, "Two-level volume rendering," *IEEE Trans. Vis. Comput. Graph.*, vol. 7, no. 3, pp. 242–252, Jul.–Sep. 2001.

[14] A. Wenger, D. F. Keefe, S. Zhang, and D. H. Laidlaw, "Interactive volume rendering of thin thread structures within multivalued scientific data sets," *IEEE Trans. Vis. Comput. Graph.*, vol. 10, no. 6, pp. 664–672, Nov.–Dec. 2004.

[15] M. Harders and G. Székely, "Enhancing human-computer interaction in medical segmentation," *Proc. IEEE*, vol. 91, no. 9, pp. 1430–1442, Sep. 2003.

[16] L. Vosilla, G. De Leo, M. Fato, A. Schenone, and F. Beltrame, "An interactive tool for the segmentation of multimodal medical images," in *Proc. IEEE Inf. Technol. Appl. Biomed.* Nov. 9–10, 2000, pp. 203–209

[17] S.-C. Yoo, C.-U. Lee, B. G. Choi, and P. Saiviroonporn, "Interactive 3-dimensional segmentation of MRI data in personal computer environment," *J. Neurosci. Methods*, vol. 112, pp. 75–82, 2001.

[18] E. Bullitt and S. R. Aylward, "Volume rendering of segmented image objects," *IEEE Trans. Med. Imag.*, vol. 21, no. 8, pp. 998–1002, Aug. 2002.

[19] K.-P. Wong, D. Feng, S. R. Meikle, and M. J. Fulham, "Segmentation of dynamic PET images using cluster analysis," *IEEE Trans. Nucl. Sci.*, vol. 49, no. 1, pt. 1, pp. 200–207, Feb. 2002.

[20] H. Guo, R. Renaut, K. Chen, and E. Rieman, "Clustering huge data sets for parametric PET imaging," *Biosystems*, vol. 71, pp. 81–92, 2003.

[21] J. G. Brankov, N. P. Galatsanos, Y. Yang, and M. N. Wernick, "Segmentation of dynamic PET or fMRI images based on a similarity metric," *IEEE Trans. Nucl. Sci.*, vol. 50, no. 5, pt. 2, pp. 1410–1414, Oct. 2003.

[22] J. Bezdek, *Pattern Recognition With Fuzzy Objective Function Algorithm*. Norwell, MA: Kluwer, 1981.

[23] X. L. Xie and G. Beni, "A validity measure for fuzzy clustering," *IEEE Trans. Pattern Anal. Mach. Intell.*, vol. 13, no. 8, pp. 841–847, Aug. 1991.

[24] S. Hu, E. A. Hoffman, and J. M. Reinhardt, "Automatic lung segmentation for accurate quantification of volumetric X-ray CT images," *IEEE Trans. Med. Imag.*, vol. 20, no. 6, pp. 490–498, Jun. 2001.

[25] D. Shreiner, M. Woo, J. Neider, and T. Davis, *OpenGL Programming Guide: The Official Guide to Learning OpenGL Version 1.4*, 4th ed. Boston, MA: Addison-Wesley, 2003.

[26] K. Jones and J. McGee, *SGI OpenGL Volumizer 2 Programmer's Guide*. Mountain View, CA: Silicon Graphics, Inc., 2004.

[27] J. Kniss, P. McCormick, A. McPherson, J. Ahrens, J. Painter, A. Keahey, and C. Hansen, "Interactive texture-based volume rendering for large data sets," *IEEE Comput. Graph. Appl.*, vol. 21, no. 4, pp. 52–61, Jul.–Aug. 2001.

[28] R. Westermann and B. Sevenich, "Accelerated volume ray-casting using texture mapping," in *Proc. IEEE Vis.,* Oct. 21–26, 2001, pp. 271–278.

[29] "ARB fragment program specification," ATI Research, Marlborough, MA, 2002.

[30] I. G. Zubal, C. R. Harrell, E. O. Smith, Z. Rattner, G. Gindi, and P. B. Hoffer, "Computerized three-dimensional segmented human anatomy," *Med. Phys.*, vol. 21, pp. 299–302, 1994.

[31] R. A. Hawkins, M. E. Phelps, and S. C. Haung, "Effects of temporal sampling glucose metabolic rates, and disruptions of the blood-brain barrier on the FDG model with and without a vascular compartment: Studies in human brain tumors with PET," *J. Cereb. Blood Flow Metab.*, vol. 6, pp. 170–183, 1986.

[32] A. P. Zijdenbos, B. M. Dawant, R. A. Margolin, and A. C. Palmer, "Morphometric analysis of white matter lesions in MR images: Methods and validation," *IEEE Trans. Med. Imag.*, vol. 13, no. 4, pp. 716–724, Dec. 1994.

[33] C. S. Patlak and R. G. Blasberg, "Graphical evaluation of blood-to-brain transfer constants from multiple-time uptake data. Generalisations," *J. Cereb. Blood Flow Metab.*, vol. 5, pp. 584–590, 1985.

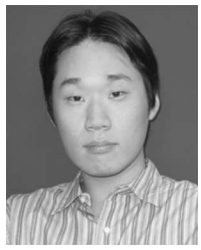

Jinman Kim (S'01–M'06) received the B.S. (honors) degree in computer science and technology in 2001 from the University of Sydney, Sydney, Australia, where he is currently working toward the Ph.D. degree in information technologies.

His research interests include the development of multidimensional image segmentation, image enhancement, information visualization, content-based image retrieval, and computer-aided diagnosis.

Weidong Cai (S'99–M'01) received the B.S. degree in Computer Science from HuaQiao University, Quanzhou, China, in 1989, and the Ph.D. degree from the University of Sydney, Sydney, Australia, in 2001, both in computer science.

Prior to his doctoral study, he worked in industry for five years. After graduation, he was a Postdoctoral Research Associate at the Centre for Multimedia Signal Processing (CMSP), Hong Kong Polytechnic University. In 2001, he was a Lecturer and is currently a Senior Lecturer in the School of Information Technologies, University of Sydney. His research interests include computer graphics, image processing and analysis, data compression and retrieval, and multimedia database and computer modelling with biomedical applications.

Stefan Eberl (M'97) received the B.E. (honors) degree in electrical engineering from New South Wales Institute of Technology, Sydney, Australia, in 1982, and the M.Sc. degree in physics and the Ph.D. degree in biomedical engineering from the University of New South Wales, Sydney, in 1997 and 2001, respectively.

He is currently a Principal Hospital Scientist in the Department of PET and Nuclear Medicine, Royal Prince Alfred Hospital, Sydney, and is an Adjunct Associate Professor in the School of Information Technologies, University of Sydney, Sydney. His research interests include physiological parameter estimation from functional imaging, image registration, and optimizing use of the combination of functional/anatomic data.

Dagan Feng (S'88–M'88–SM'94–F'03) received the M.E. degree in electrical engineering and computing science from Shanghai JiaoTong University, Shanghai, China, in 1982, and the M.Sc. degree in biocybernetics and the Ph.D degree in computer science from the University of California, Los Angeles, in 1985 and 1988, respectively.

After briefly working as an Assistant Professor at the University of California, Riverside, he joined the University of Sydney, Sydney, Australia, at the end of 1988, where he was a Lecturer, Senior Lecturer, Reader, Professor, Head of Department of Computer Science, Head of School of Information Technologies, and is currently Associate Dean of the Faculty of Science. He is also the Honorary Research Consultant, Royal Prince Alfred Hospital, Sydney; the Chair-Professor of Information Technology, Hong Kong Polytechnic University, Hong Kong; the Advisory Professor, Shanghai JiaoTong University; and a Guest Professor with Northwestern Polytechnic University, Xian, China, with Northeastern University, Shenyang, China, and with Tsinghua University, Beijing China. He is the Founder and Director of the Biomedical and Multimedia Information Technology Research Group. He has published over 400 scholarly research papers, pioneered several new research directions, and made a number of landmark contributions in his field with significant scientific impact and social benefit. His research area is biomedical and multimedia information technology.

Dr. Feng is a Fellow of the Australia Computer Society, the Australian Academy of Technological Sciences and Engineering, Hong Kong Institution of Engineers, and the Institution of Electrical Engineers, U.K. He is also the special Area Editor of the IEEE TRANSACTIONS ON INFORMATION TECHNOLOGY IN BIOMEDICINE and is the current Chairman of IFAC-TC-BIOMED. He is the recipient of the Crump Prize for Excellence in Medical Engineering (USA).